

Communication

Intergranular Crack of Cathode Materials in Lithium-Ion Batteries Subjected to Rapid Cooling During Transient Thermal Runaway

Siqi Li ¹, Changchun Ye ¹, Ming Jin ², Guobin Zhong ^{2,3}, Shi Liu ^{2,3,*}, Yajie Liu ^{1,*}  and Zhixin Tai ^{1,*}

¹ Advanced Energy Storage Materials and Technology Research Center, Guangdong-Hong Kong Joint Laboratory for Carbon Neutrality, Jiangmen Laboratory of Carbon Science and Technology, Jiangmen 529199, China; lisiqi@hkustgz-jcl.ac.cn (S.L.); yechangchun@hkustgz-jcl.ac.cn (C.Y.)

² National Institute of Guangdong Advanced Energy Storage, Guangzhou 510080, China; jinming@naesic.com (M.J.); zhongguobin@naesic.com (G.Z.)

³ China Southern Power Grid Technology Co., Ltd., Guangzhou 510062, China

* Correspondence: liushi@naesic.com (S.L.); liuyajie@hkustgz-jcl.ac.cn (Y.L.); taizhixin@hkustgz-jcl.ac.cn (Z.T.)

Abstract

In metallurgy, the quenching process often induces changes in certain material properties, such as hardness and ductility, through the rapid cooling of a workpiece in water, gas, oil, polymer, air, or other fluids. Given that lithium-ion batteries operate under relatively benign conditions, conventional rapid cooling does not significantly affect the property variations in their internal electrode materials during normal use. However, thermal runaway presents an exception due to its dramatic temperature fluctuations from room temperature to several hundred degrees Celsius. In this study, we investigated NCM811 cathodes in 18,650 batteries subjected to transient thermal runaway followed by rapid cooling using several advanced analytical techniques. The results reveal a phenomenon characterized by intergranular cracking within NCM811 cathode materials when exposed to rapid cooling during transient thermal runaway. Furthermore, lithium-ion cells utilizing reused NCM-182.4 electrodes in fresh electrolyte demonstrate a reversible capacity of 231.4 mAh/g after 30 cycles at 0.1 C, highlighting the potential for reusing NCM811 cathodes in the lithium-ion battery recycling process. These findings not only illustrate that NCM811 particles may experience intergranular cracking when subjected to rapid cooling during transient thermal runaway, but also the rapidly cooled NCM811 electrodes exhibit potential for reuse.

Keywords: granular crack; thermal runaway; cathode



Academic Editor: Yong-Joon Park

Received: 6 August 2025

Revised: 16 September 2025

Accepted: 26 September 2025

Published: 30 September 2025

Citation: Li, S.; Ye, C.; Jin, M.; Zhong, G.; Liu, S.; Liu, Y.; Tai, Z. Intergranular Crack of Cathode Materials in Lithium-Ion Batteries Subjected to Rapid Cooling During Transient Thermal Runaway. *Batteries* **2025**, *11*, 363. <https://doi.org/10.3390/batteries11100363>

Copyright: © 2025 by the authors. Licensee MDPI, Basel, Switzerland. This article is an open access article distributed under the terms and conditions of the Creative Commons Attribution (CC BY) license (<https://creativecommons.org/licenses/by/4.0/>).

1. Introduction

As the rapid development of electric vehicles and large-scale energy storage systems continues, there is an increasing global demand for the recycling of lithium-ion batteries (LIBs). This demand arises from the necessity for sustainable energy storage solutions and the environmental challenges associated with battery waste disposal [1–3]. Although retirement standards for LIBs are mandated based on various key characteristics, such as cycle conditions, ambient temperature, charge and discharge rates, and voltage, batteries that have experienced thermal runaway (TR) must be disposed of. Thermal runaway is considered an irreversible failure mode that can lead to catastrophic consequences. During this event, a battery undergoes specific types of abuse including mechanical, electrical, and

thermal abuse [4–6]. Consequently, LIBs that have undergone cooling and fire extinguishing treatments following fire incidents must be directed to recycling lines designated for spent LIBs.

In recycling industry, the cathode materials within the spent LIBs, including lithium nickel–cobalt–manganese oxide (NCM)cathodes, LiCoO_2 , LiMn_2O_4 , $\text{Li}(\text{CoNiMn})\text{O}_2$, and LiFePO_4 are transformed into alloys containing Li, Ni, Mn and Co elements by utilization of pyrometallurgy or biohydrometallurgy processes [7–10]. They are always accompanied by significant investment into equipment, energy-wasting, and heavy pollution. In pyrometallurgy, spent LIBs are often heated at low temperatures of 150 to 500 °C to evaporate electrolyte, and then at relatively high temperatures of 1400 to 1700 °C to melt and recover Co, Ni, Cu, and Fe. Thus, a lot of energy is required to transform these elements into their alloys [11–13]. During heat treatment conducted as a part of the regeneration procedure, these materials spontaneously generate secondary pollutions, including SO_2 , Cl_2 , NO_x , and so on, which easily leads to the greenhouse effect [14]. Thus, a thought-provoking question is raised regarding the appropriate management of such lithium-ion batteries (LIBs) that are in relatively good condition but have experienced transient thermal runaway followed by rapid extinguishment.

As a battery undergoes thermal runaway, it generates high-temperature gases, resulting in a rapid increase in temperature [15]. During the subsequent extinguishment process, the batteries experience a swift transition from elevated temperatures to room temperature upon exposure to an extinguishing agent. In this process, both the cathode materials and other battery components undergo a critical heat treatment, like “quenching”, accompanied by rapid cooling. However, this quenching technology has emerged as an innovative pathway for regulating surface and interface structures in nanomaterials [16,17]. It has been effectively employed in nanomaterial synthesis, facilitating rapid cooling to control these structural characteristics [18]. As a battery experiences thermal runaway, it produces high-temperature gases, leading to a rapid increase in temperature. During the subsequent extinguishment process, the batteries, as well as electrode materials, separators, and residual electrolytes, undergo a swift transition from elevated temperatures to room temperature when exposed to an extinguishing agent. In this process, the cathode materials and other battery components undergo a critical heat treatment known as “quenching,” followed by rapid cooling. As an emerging method for regulating surface and interface properties in nanomaterials, this quenching technology has been utilized in the synthesis of nanomaterials, facilitating rapid cooling to effectively control their surface and interface structures [19]. Our previous research on the quenching engineering of nanomaterials has demonstrated a reliable capability for surface and interface regulation in core–shell catalysts [20,21]. This includes enhanced lattice distortion, increased defects, and greater heteroatom doping. Consequently, this innovative technology shows significant promise in the enhancement of nanomaterials as well as in the recycling of cathode materials from spent lithium-ion batteries.

In this study, we report a phenomenon involving intergranular cracking in the cathode materials ($\text{LiNi}_{0.8}\text{Co}_{0.1}\text{Mn}_{0.1}\text{O}_2$, NCM811) of lithium-ion batteries subjected to rapid cooling during transient thermal runaway events. The varying stress experienced by NCM811 particles may be attributed to volume changes resulting from the deterioration of their crystal structure during the rapid cooling process. Upon reintroducing fresh electrolyte, the NCM-182.4 (denoting samples treated at 182.4 °C) electrode exhibits an enhanced lithium-ion storage capability compared to the NCM-25 electrode, achieving a reversible capacity of 231.4 mAh/g after 30 cycles at a rate of 0.1 C, which corresponds to a capacity retention of approximately 89.8%. These findings indicate that intergranular cracking in NCM811 particles can occur when these batteries are exposed to rapid cooling during transient

thermal runaway events. This is likely due to stress differences arising from volume changes linked to surface crystal structure degradation in the NCM811 particles. This study presents a novel strategy for repurposing NCM811 electrodes from waste batteries within the battery recycling process.

2. Materials and Methods

2.1. Materials

In this study, 18,650 batteries constructed with $\text{LiNi}_{0.8}\text{Co}_{0.1}\text{Mn}_{0.1}\text{O}_2$ (NCM811) and graphite electrodes, along with a polyethylene (PE) separator, are examined under various experimental temperatures of 25 °C, 165 °C, 182.4 °C, and 195 °C. To minimize the impact of battery inconsistency, all batteries used in the experiment were initially discharged to 2.5 V and subsequently charged to 3.7 V at a current density of 1 A. This process was repeated for at least three cycles. Prior to testing, all batteries were charged to a state of charge (SOC) of 50% at a rate of 1 A using constant current and constant voltage settings of 3.4 V, followed by maintenance in a relatively stable environment at an ambient temperature of 25 °C and humidity level of 65% for a duration of 24 h.

2.2. Experimental Design

The 18,650 batteries are heated at 10 °C/min to 25 °C, 165 °C, 182.4 °C and 195 °C, respectively. These samples are designated as NCM-25, NCM-165, NCM-182.4, and NCM-195, respectively. Subsequently, all the batteries are kept at the set temperature for 10 min and then, CO_2 (2.5 MPa) as fire extinguishing agent was discharged during the cooling down process of batteries to 25 °C. Figure 1a presents the schematic of the thermal runaway and the process of cooling down in the current study. To confirm obtaining reliable measurement results, all the aforementioned tests were repeated at least three times, and the standard deviations of the critical parameters, including surface temperature, heat release rate, mass loss and so on, were kept at less than 13.5%. Here, three K-type thermocouples were fixed on the surface of the batteries to record the involution of the temperature. The CO_2 was applied at a flow rate of 0.67 kg/min for a duration of 10 s, and the distance between the nozzle and the surface of battery cell was kept at 30 mm. An electric heater with the rated power of 0.65 KW and the rectangular heating size of 100 mm × 100 mm was placed along the flank of the batteries. The surface temperature of the batteries was recorded at the heating power rate of 100 W for the thermal runway property test. An electric balance with a measuring precision of 0.01 g was employed to record the change in the mass of the batteries. As shown in Figure 1b, the resulting 18,650 batteries are dismantled in a glovebox filled by argon ($\text{H}_2\text{O} < 0.01 \text{ ppm}$, $\text{O}_2 < 0.01 \text{ ppm}$). After drying for 12 h, the NMC electrode was cut into a disk with a diameter of 12 mm for further battery tests.

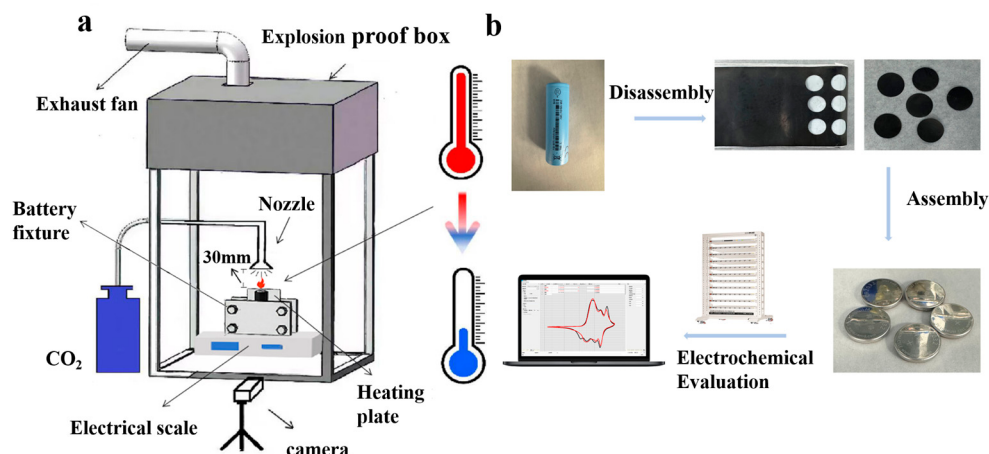


Figure 1. Schematic illustration of the process of lithium-ion batteries subjected to transient thermal runaway from high temperature to room temperature (a) and electrochemical test (b) of their cathode electrodes as they cool down to ambient temperature, experiencing the extinguishment by utilization of CO₂.

2.3. Characterization and Electrochemical Tests

The crystal structure of the as-prepared products was determined using a Rigaku SmartLab SE Automated Multipurpose X-ray diffractometer (XRD) with Cu K α radiation ($\lambda = 0.15406$ nm). Scanning electron microscopy (SEM) images were obtained using a Phenom Pro Desktop microscope from the USA. Transmission electron microscopy (TEM) and high-resolution transmission electron microscopy (HRTEM) analyses were conducted on a JEM-F200 transmission electron microscope. The thermal stability of the samples was evaluated through thermogravimetric analysis (TGA, NETZSCH STA449C) in air at a heating rate of $10\text{ }^{\circ}\text{C min}^{-1}$. The lithium storage performance was assessed utilizing CR2032 type coin cells. A homemade lithium metal foil served as the anode, while 1 M LiPF₆ in ethylene glycol dimethyl ether (DME) functioned as the electrolyte. Additionally, a commercial polyethylene separator (Celgard 2400, Suzhou Shengernuo Technology Co., Ltd., China.) was employed within these cells. The assembly process for the coin cells took place in a high-purity argon glove box, maintaining H₂O levels below 0.01 ppm and O₂ levels below 0.01 ppm. The mass loading of active anode material for each half-cell was controlled to be approximately 0.7–1.1 mg/cm². The cells underwent testing on battery testers (NEWARE), operating within a voltage window of 2.5–4.5 V versus Li⁺/Li. Cyclic voltammetry (CV) tests were performed using a BioLogic VMP3 over a voltage range of 2.5–3.7 V, while electrochemical impedance spectroscopy (EIS) analysis was also conducted by Biologic, with scanning frequencies ranging from 0.01 Hz to 10⁵ Hz and an applied voltage amplitude of ± 10 mV.

3. Results and Discussion

The general thermal runaway behavior of 18,650 batteries is investigated in detail. As illustrated in Figure 2a, the thermal runaway process can be categorized into four critical stages based on temperature thresholds of 95.3 °C, 124.3 °C, and 209.2 °C, alongside observations of battery appearance and elevated temperature rates [22,23]. In Stage 1, the surface temperature of the battery rises gradually. However, changes in volume (Figure 2b) and physical appearance (as depicted in Figure S1) are not readily observable. Upon reaching a temperature of 95.3 °C (Figure S2), the battery begins to swell. As the temperature further increases, the electrolyte reaches its boiling point, which subsequently leads to the rupture of the safety valve due to significant gas release. Stage 3 is characterized by a rapid increase in surface temperature up to 209.2 °C, indicating substantial energy generation resulting

from both separator decomposition and internal micro-short circuits [24,25]. During this stage, as heating rate approaches approximately $1.0\text{ }^{\circ}\text{C/s}$ around a temperature of $180\text{ }^{\circ}\text{C}$, self-heating predominates over other factors contributing to an abrupt rise in battery temperature towards its peak. The obvious fluctuations in the temperature rise rate, with the temperature rise rate $dT/dt \geq 1\text{ }^{\circ}\text{C/s}$ and a duration of more than 3 s, indicated that the thermal runaway process transitions from a gradual accumulation stage to a sudden, violent, and irreversible self-acceleration stage [26]. Therefore, $182.4\text{ }^{\circ}\text{C}$ was selected as the critical temperature point in this research. In Stage 4, as the temperature exceeds $209.2\text{ }^{\circ}\text{C}$, the battery experiences large-scale short-circuiting (Figure 2b), and oxygen release occurs along with electrolyte combustion. Additionally, melting aluminum-plastic films lead to flame ejection, culminating in significant mass loss (Figure 2c) [27,28]. Notably, a threshold of special significance is observed at approximately $180\text{ }^{\circ}\text{C}$, and after that, the rate of temperature increase reaches about $1\text{ }^{\circ}\text{C/s}$, indicating that self-accelerated heat release initiates prior to ignition [29,30]. Furthermore, as shown in Figure 2c, there is only minimal mass loss ($\sim 10\text{ wt.}\%$) in the temperatures ranging from ambient conditions up to around $200\text{ }^{\circ}\text{C}$, suggesting that electrode integrity remains largely intact throughout this range.

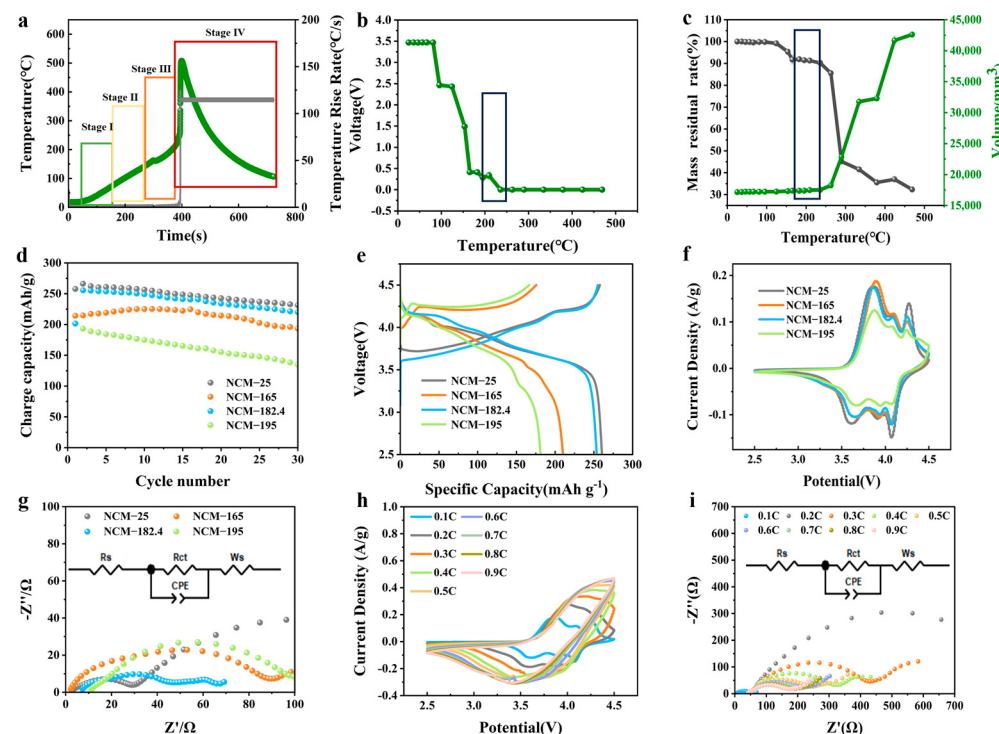


Figure 2. Thermal runaway properties. (a) Temperature variation curves of the middle part in the battery versus time during the thermal runaway process. (b) Open circuit voltage (OCV) involution as the temperature increases. (c) Mass residual rate and the corresponding volume change from room temperature to $468.8\text{ }^{\circ}\text{C}$. The electrochemical performance of NCM811 subject to cooling down followed a 10 minutes' thermal treatment at $25\text{ }^{\circ}\text{C}$, $165\text{ }^{\circ}\text{C}$, $182.4\text{ }^{\circ}\text{C}$ and $195\text{ }^{\circ}\text{C}$, respectively. (d) Long-term cycling at 0.1 C ($1\text{ C} = 280\text{ mAh/g}$). (e) Charge–discharge voltage profiles at 0.1 C . (f) Cyclic voltammograms between 2.5 V and 4.5 V . (g) EIS plots of four NCM electrodes in batteries after CV measurements. (h) CV curves of NCM-182.4 electrode in batteries with various scan rates from 0.1 mV/s to 0.9 mV/s between 2.5 V and 4.5 V . (i) The corresponding EIS plots after CV measurements.

To evaluate the electrochemical performance of the NCM811 electrodes subjected to thermal impact for approximately 10 min, a half-cell configuration was employed to investigate their lithium-ion storage properties. Figure 2d illustrates the stability over 30 cycles at a current density of 0.1 C within a voltage range of 2.5 V to 4.5 V . In comparison

with other NCM811 electrodes, NCM-25 demonstrates relatively stable cycling performance, achieving a reversible capacity of 231.4 mAh/g after 30 cycles at 0.1 C, which corresponds to a capacity retention of approximately 89.8%. Notably, despite thermal treatment, NCM-182.4 exhibits superior cycling stability compared to both NCM-165 and NCM-195.

Furthermore, the corresponding galvanostatic charge/discharge (GCD) profiles at a rate of 0.1 C (Figure S7) indicate that the NCM-182.4 electrode exhibits voltage plateaus, which are highly comparable to those of NCM-25, suggesting similar electrochemical reactions during the lithium-ion charge–discharge process. Figure 2f further illustrates this phenomenon, showing that all NCM811 electrodes display analogous oxidation and reduction peaks: a prominent peak at 3.86 V, which corresponds to the oxidation of Ni^{2+} to $\text{Ni}^{3+}/\text{Ni}^{4+}$, along with two less pronounced peaks at 4.09 V and 4.24 V associated with the oxidation of Co^{3+} to Co^{4+} reactions. In Figure 2h, cyclic voltammograms for NCM-182.4 across scan rates from 0.1 C to 0.9 C underscore its excellent C-rate capability. As depicted in Figure 2g, electrochemical impedance spectroscopy (EIS) reveals that NCM-182.4 demonstrates lower interfacial electric resistance (approximately $84.1\ \Omega$) compared to NCM-165 (around $101\ \Omega$) and NCM-195 (approximately $112\ \Omega$).

Moreover, Figure 2i illustrates the evolution of charge-transfer resistance (R_{ct}) as observed in their electrochemical impedance spectroscopy (EIS) measurements across various scan rates ranging from 0.1 C to 0.9 C. The R_{ct} initially increases during the early cycles at 0.1 and 0.2 C; however, this value subsequently decreases with increasing scan rates, indicating the formation of a series of novel interfaces on the surface of the recycled NCM811 electrode. Specifically, based on EIS fitting results obtained through software analysis, it is evident that at least three semicircles are present in the EIS data, corresponding to different R_{ct} values ($11.77\ \Omega$, $84.09\ \Omega$, and $108.79\ \Omega$). These findings suggest that there may be a deeper scientific issue underlying this intriguing phenomenon.

To investigate the differences between NCM-25 and NCM-182.4, their TEM images are presented in Figure 3a,b. Although NCM-182.4 was heated at $182.4\ ^\circ\text{C}$ for 10 min, it remains evident that a cathode electrolyte interface (CEI) has formed on the surface of the NCM811 samples, with its thickness approaching that of NCM-25. In comparison to the EDS mapping images of NCM-25 shown in Figure 3, as well as considering brightness levels, the spot densities corresponding to chemical elements such as Co, Ni, and Mn in NCM-182.4 are higher than those observed in NCM-25. This variation may be attributed to differences in CEI thickness on the surfaces of the NCM811 samples. It is a common method to use EDX for evaluating CEI [31,32]. For example, Wang et al. used EDX at 5–10 kV and a silicon drift detector (SDD) to map the distribution of fluorine and phosphorus in CEI, with a fixed dwell time of 60 s per point [33]. Huang et al. used a low-kV (5 kV) EDX setup and a large-area detector to improve sensitivity for light elements in CEI [34]. Furthermore, this residual CEI film could contribute to the formation of complex CEI films during the initial charge–discharge cycles previously observed.

To gain deeper insight into the underlying mechanisms for the increased Li-ion storage capability for NCM811 samples, a series of structural characterization were conducted to examine their microstructure. X-ray diffraction (XRD) was employed to analyze the crystal structure of NCM811 samples at various temperatures following the rapid cooling process. Figure 4a exhibits the X-ray diffraction patterns of NCM samples from $25\ ^\circ\text{C}$ to $190\ ^\circ\text{C}$. The NCM-25 exhibits a typical hexagonal a-NaFeO₂ layered structure (R-3m space group, PDF#74-0919). As the temperature of the thermal treatment increases, the peak of (003) crystal plane of the NCM-165 shows a slight red shift, indicating that the interplanar spacing of (003) crystal plane increases, which may be a result of lattice expansion. As the temperature reaches $182.4\ ^\circ\text{C}$, the sharp peak (003) turns into a broad peak compared to NCM-165, and with the temperature increasing, the peak width is still maintainedIt

should be noted that this involution of X-ray diffraction patterns of NCM811 may be a result of crystal structure deterioration. In Figure S6, based on the Scherrer equation, $D = K\lambda/(\beta \cos \theta)$, where K is the shape factor (0.89), λ is the X-ray wavelength, and θ is the Bragg angle, the grain sizes were acquired as 1.1029 nm (NCM-25), 1.0372 nm (NCM-182.4-natural cooling) and 0.4743 nm (NCM-182.4-rapid cooling), respectively. The results indicate that the grain size (D) of the rapidly cooled sample is smaller than that of the naturally cooled sample.

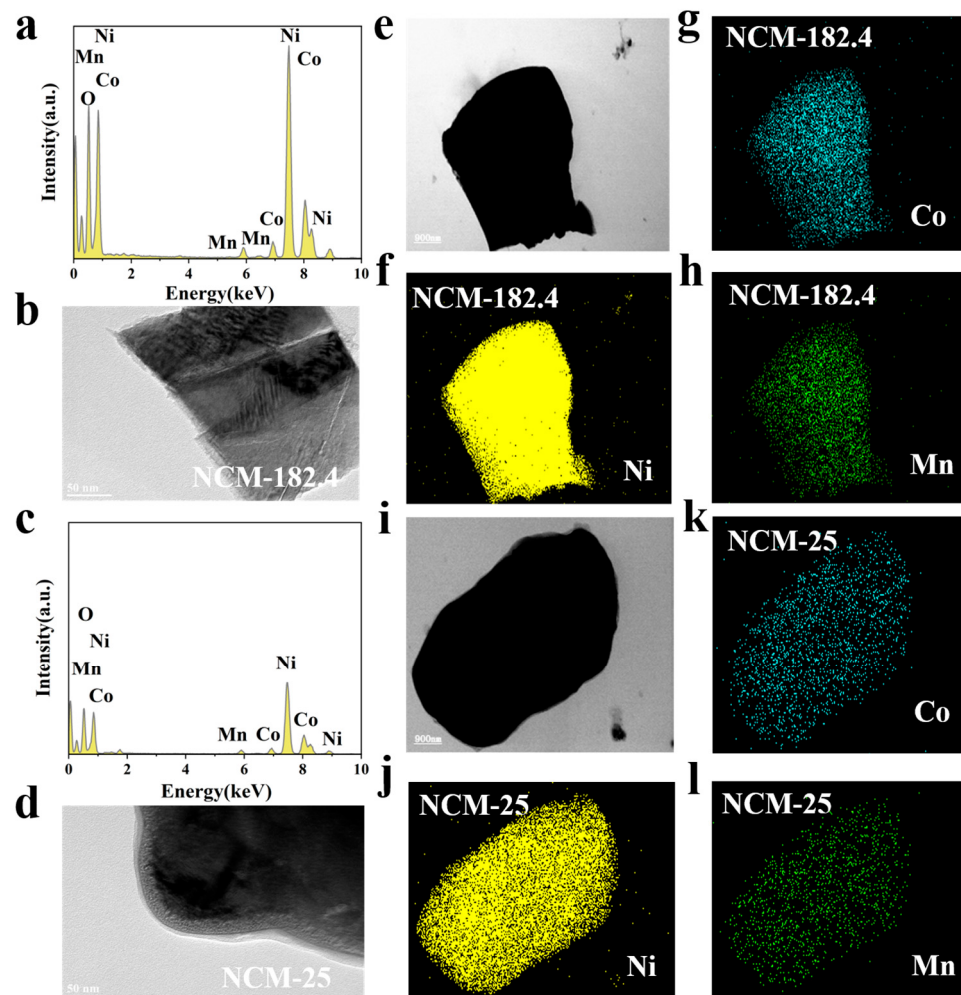


Figure 3. EDX spectrum of (a) NCM-182.4 and (c) NCM-25, TEM image of (b) NCM-182.4 and (d) NCM-25, and EDS mapping of the distribution of Co, Ni, and Mn elements in (e–h) NCM-182.4 and (i–l) NCM-25, respectively.

Selected area electron diffraction (SAED) was used to further verify their crystal structure at both the surface and internal of NCM811 particles. As shown in Figure 3g,h, the SAED images of NCM-182.4 exhibit an obvious trend towards regular diffraction cycles, indicating the formation of abundant randomly oriented small grains. In comparison, the NCM-25 shows single-oriented single crystals or large grains due to its diffraction spots. Based on the experimental evidence, it can be inferred that the change in crystal may be attributed to the crystal structure deferrization of NCM811.

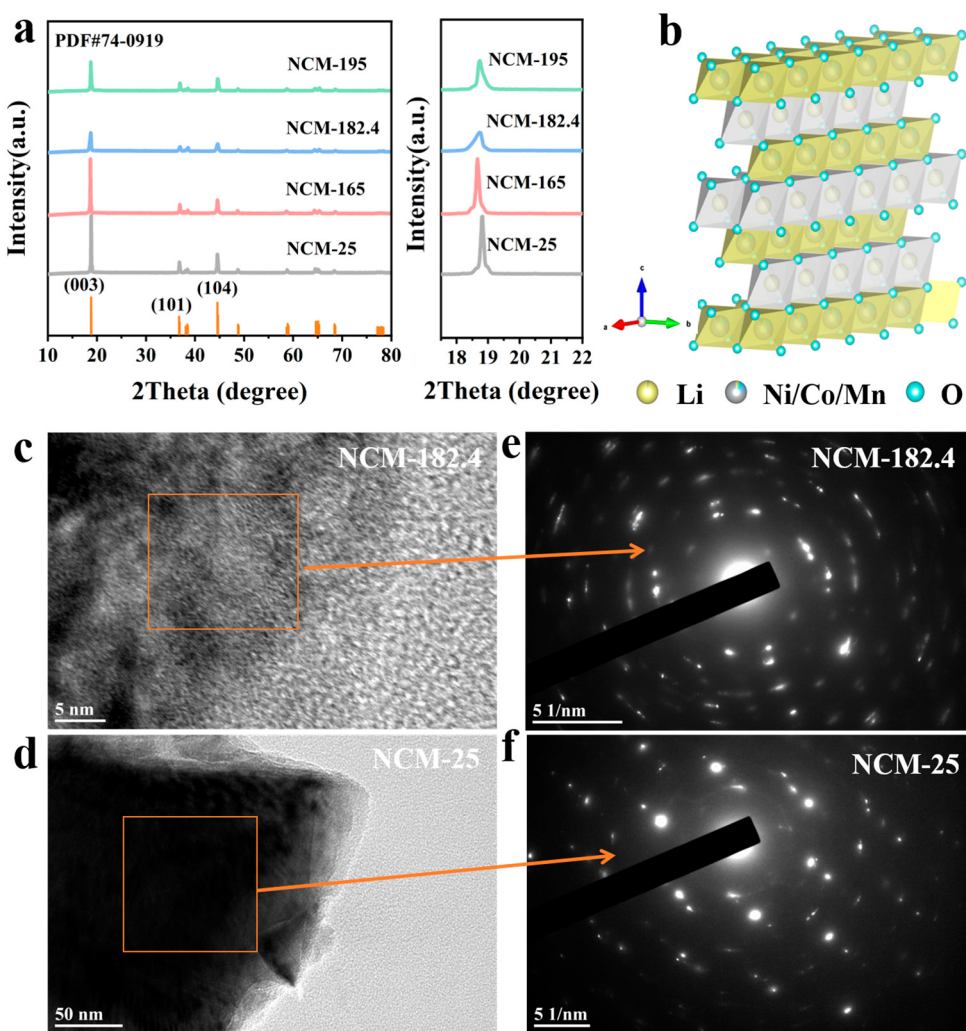


Figure 4. Structural characterization of NCM811 samples subject to thermal treatment at different temperatures using CO₂. **(a)** Phase and structure evolution with the increase in temperature. And their enlarged perspective between 18 and 19.5 degrees. **(b)** Crystal structure of the NCM811. TEM images of **(c)** NCM-182.4 and **(d)** NCM-25, and their corresponding SAED patterns of **(e)** NCM-182.4 and **(f)** NCM-25.

The scanning electron microscope (SEM) was utilized to examine the morphology of NCM811 samples. In Figure 5a,b, NCM-25 and NCM-165 exhibit distinct spherical shapes with a diameter of 10.2 μm . As the thermal temperature rises to 182.4 °C, the NCM-182.4 sample reveals an abundance of half-spheres or smaller fragments, as shown in Figure 5c. With further increases in temperature, NCM-195 displays both spherical particles and fragments. This phenomenon indicates significant morphological changes in the NCM811 samples when subjected to thermal treatment followed by rapid cooling using CO₂. The presence of cracks within the NCM811 particles can be attributed to several factors, including lattice collapse, phase transformation, cation disorder, loss of lattice oxygen, surface reconstruction, and heterogeneous lithiation/delithiation processes. Notably, these fracture surfaces demonstrate a fine crystalline structure akin to that observed in metal materials after quenching. Drawing inspiration from research on metal quenching, it can be inferred that these fractures are linked to alterations in crystal structure which often result from variations in internal stress. The formation of such cracks is primarily driven by random crystal orientations among particles; this randomness may lead to anisotropic volume changes during the rapid cooling process facilitated by CO₂.

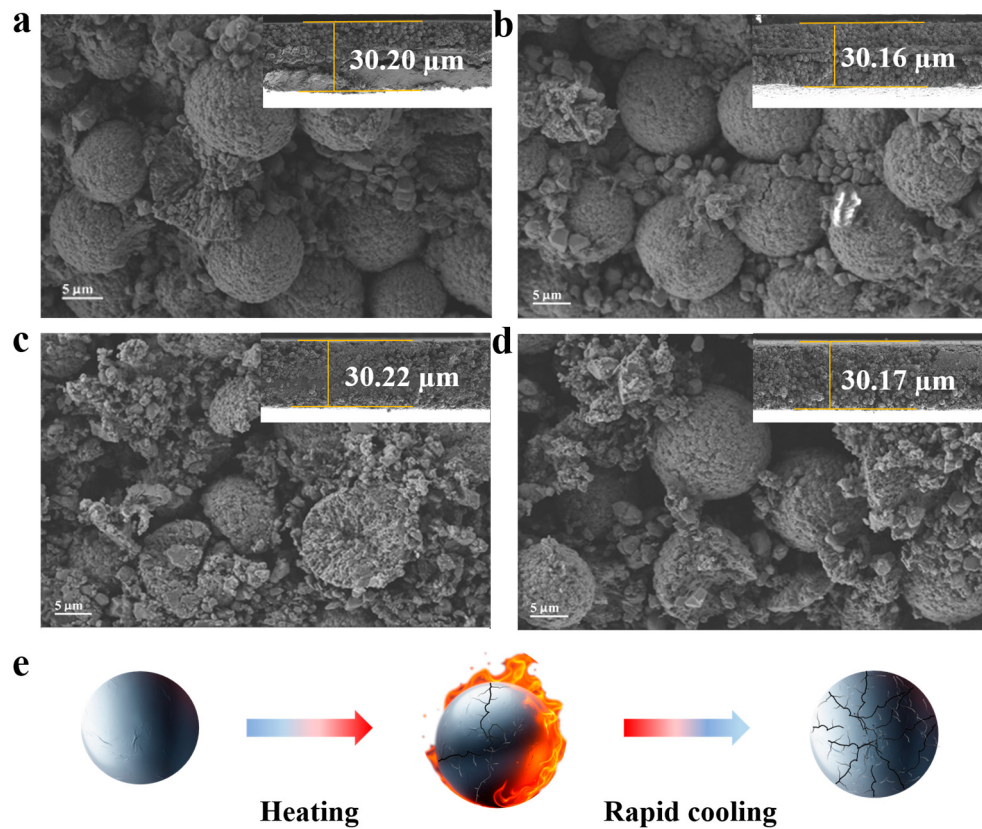


Figure 5. Zoom-in view and the inset overall view of the cross-section for NCM811 samples following thermal treatment and rapid cooling process. (a) NCM-25, (b) NCM-165, (c) NCM-182.4 and (d) NCM-195 electrode before cycling. (e) The proposed diagram of intergranular involution process.

To further mitigate the effects of thermal treatment, a sample subjected to thermal processing at 182.4 °C for 10 min, followed by a cooling rate of 1 °C/min, was prepared as a reference for scanning electron microscopy (SEM) observation and battery testing. As illustrated in Figure S4, compared to NCM-182.4, the NCM811 sample that underwent slow cooling treatment exhibits a more pronounced micro-sized sphere-like morphology with fewer fragments. Additionally, its lithium storage capacity is lower than that of the NCM-182.4 sample, depicted in Figure S5. These findings underscore the critical role of rapid cooling treatment in facilitating the rupture of NCM811 samples. Moreover, when compared to other samples, the thickness of approximately 30.22 μm observed in NCM-182.4 shows only slight variation according to their inset images, indicating that the rupture process in NCM811 samples does not lead to an increase in the overall volume of the electrode. Thus, it can be inferred that these NCM811 spheres maintain their original spherical shape while exhibiting intergranular cracks within the electrode (as depicted in Figure 5e), thereby preserving electrical contact between electrodes and active materials. As this electrode was reused and re-wetted with fresh electrolyte, these small fragments could function as submicron or nanosized particles capable of enhancing lithium-ion storage capacity.

4. Conclusions

In this study, we report the occurrence of intergranular cracking in NCM cathode materials used in lithium-ion batteries subjected to rapid cooling during transient thermal runaway. The results indicate that rapid cooling induces intergranular cracks when the NCM reaches a temperature of 182.4 °C, attributed to the internal stress differences between the interior and surface of NCM811 particles. This differential stress may arise from volume

changes caused by crystal structure deterioration during the rapid cooling process. Upon reintroducing fresh electrolyte, the NCM-182.4 electrode exhibits enhanced lithium-ion storage capabilities compared to the NCM-25 electrode, achieving a reversible capacity of 231.4 mAh/g after 30 cycles at a rate of 0.1 C, which corresponds to a capacity retention of approximately 89.8%. These findings suggest that intergranular cracking in NCM811 particles can occur when these batteries are exposed to rapid cooling during transient thermal runaway, providing a novel strategy for recycling waste batteries within battery recycling processes.

Supplementary Materials: The following supporting information can be downloaded at <https://www.mdpi.com/article/10.3390/batteries11100363/s1>; Figure S1: The images of 18,650 NCM battery undergo rapid cooling under various conditions. (a), 25 °C, (b), 36.3 °C, (c), 46.3 °C, (d), 56.3 °C, (e), 66.3 °C, (f), 80.8 °C, (g), 95.3 °C, (h), 124.3 °C, (i), 153.4 °C, (j), 165 °C, (k), 182.4 °C, (l), 195 °C, (m), 209.2 °C, (n), 235.9 °C, (o), 262.7 °C, (p), 289.4 °C, (q), 334.3 °C, (r), 379.1 °C, (s), 424 °C, (t) and 468.8 °C, respectively; Figure S2: Images of safety valves installed on (a) NCM-25 and (b) NCM-95.3 batteries. Here, although the batteries begin to expand since 95.3 °C, their safety valves are still undamaged; Figure S3: Electrochemical impedance spectroscopy (EIS) of the batteries using reused NCM electrodes after 1st cycles; Figure S4: The morphology of NCM811 samples underwent natural (slow) cooling treatment at (a) high-magnification and (b) low-magnification; Figure S5: (a) Long-cycle stability and their charge and discharge curves at 1st cycles of the NCM-182.4 batteries after rapid and natural (slow) cooling treatments. Figure S6. Comparative XRD results of natural-cooled and rapid-cooled samples. Figure S7. The preparation process of EDX samples. Sample preparation was carried out in a strict standard operating procedure (Figure S7), and consistent parameters were used throughout the measurement process: an Oxford MAX energy-dispersive X-ray spectrometer equipped with a Be window detector (detector area: 80 mm²) was used, with a detector dead time maintained between 10% and 30%. The scan step size was set to 5 nm, corresponding to an acquisition pixel matrix of 256 × 256. Depending on the analysis area, the total acquisition time was kept within 3 min. Therefore, the measurement results are unaffected by variations in measurement conditions and sample state. Table S1. EIS fitting results corresponding to the Nyquist plot in Figure 2g. Table S2. EIS fitting results corresponding to the Nyquist plot in Figure 2i.

Author Contributions: Conceptualization, S.L. (Siqi Li), C.Y., S.L. (Shi Liu) and Y.L.; Investigation, S.L.; Validation, M.J. and Y.L.; Writing—original draft preparation, S.L.; Writing—review and editing, G.Z. and Z.T. All authors have read and agreed to the published version of the manuscript.

Funding: This research was funded by the Guangdong S&T Programme (No. 2023B0909060004).

Data Availability Statement: The original contributions presented in this study are included in the article and Supplementary Materials. Further inquiries can be directed to the corresponding author.

Conflicts of Interest: Authors G.Z. and S.L. were employed by the company China Southern Power Grid Technology Co., Ltd. The remaining authors declare that the research was conducted in the absence of any commercial or financial relationships that could be construed as a potential conflict of interest.

References

1. Jenis, P.; Zhang, T.; Ramasubramanian, B.; Lin, S.; Rayavarapu, P.R.; Yu, J.; Ramakrishna, S. Recent progress and hurdles in cathode recycling for Li-ion batteries. *Circ. Econ.* **2024**, *3*, 100087. [[CrossRef](#)]
2. Wang, T.; Luo, H.; Bai, Y.; Li, J.; Belharouak, I.; Dai, S. Direct Recycling of Spent NCM Cathodes through Ionothermal Lithiation. *Adv. Energy Mater.* **2020**, *10*, 2001204. [[CrossRef](#)]
3. Abdalla, A.M.; Abdullah, M.F.; Dawood, M.K.; Wei, B.; Subramanian, Y.; Azad, A.T.; Nourin, S.; Afroze, S.; Tawee Kun, J.; Azad, A.K. Innovative lithium-ion battery recycling: Sustainable process for recovery of critical materials from lithium-ion batteries. *J. Energy Storage* **2023**, *67*, 107551.
4. Guo, A.; Xing, Z.; Liu, Y.; Lu, W.; Wang, A.; Wu, J.; Chai, G.; Shi, Y.; Jiang, J.; Ma, Y. The disassembly analysis and thermal runaway characteristics of NCM811 family battery cells. *J. Therm. Anal. Calorim.* **2024**, *150*, 141–149. [[CrossRef](#)]

5. Zhang, W.; Zhang, J.; Hu, Y.; Zhang, L.; Zhang, W.; Chen, Y.; Zhang, G.; Jiang, L.; Dai, Z.; Wen, Y. Investigations on the essential causes of the degrading properties of ternary lithium-ion batteries with different nickel content during thermal runaway stage. *Int. J. Electrochem. Sci.* **2024**, *19*, 100491. [[CrossRef](#)]
6. Liu, Y.; Liu, J.; Zhao, Z.; Ma, Y.; Duan, Q.; Li, H.; Sun, J.; Wang, Q. The efficiency of dodecafluoro-2-methylpentan-3-one in suppressing NCM 811 lithium-ion battery fire. *Process Saf. Environ. Prot.* **2024**, *186*, 1432–1446. [[CrossRef](#)]
7. Binder, J.O.; Culver, S.P.; Zeier, W.G.; Janek, J. A Rapid and Facile Approach for the Recycling of High-Performance $\text{LiNi}_{1-x-y}\text{Co}_x\text{Mn}_y\text{O}_2$ Active Materials. *ChemSusChem* **2021**, *14*, 441–448. [[CrossRef](#)]
8. Li, L.; Bian, Y.; Zhang, X.; Xue, Q.; Fan, E.; Wu, F.; Chen, R. Economical recycling process for spent lithium-ion batteries and macro- and micro-scale mechanistic study. *J. Power Sources* **2018**, *377*, 70–79. [[CrossRef](#)]
9. Gao, S.; Feng, X.; Lu, L.; Kamyab, N.; Du, J.; Coman, P.; White, R.E.; Ouyang, M. An experimental and analytical study of thermal runaway propagation in a large format lithium ion battery module with NCM pouch-cells in parallel. *Int. J. Heat Mass Transf.* **2019**, *135*, 93–103. [[CrossRef](#)]
10. Hu, J.; Tang, X.; Zhu, X.; Liu, T.; Wang, X. Suppression of thermal runaway induced by thermal abuse in large-capacity lithium-ion batteries with water mist. *Energy* **2024**, *286*, 129669. [[CrossRef](#)]
11. Zhou, M.; Li, B.; Li, J.; Xu, Z. Pyrometallurgical Technology in the Recycling of a Spent Lithium Ion Battery: Evolution and the Challenge. *ACS ES&T Eng.* **2021**, *1*, 1369–1382. [[CrossRef](#)]
12. Yoo, E.; Lee, U.; Kelly, J.C.; Wang, M. Life-cycle analysis of battery metal recycling with lithium recovery from a spent lithium-ion battery. *Resour. Conserv. Recycl.* **2023**, *196*, 107040. [[CrossRef](#)]
13. Zhao, L.; Li, W.; Luo, W.; Zheng, M.; Chen, M. Numerical study of critical conditions for thermal runaway of lithium-ion battery pack during storage. *J. Energy Storage* **2024**, *84*, 110901. [[CrossRef](#)]
14. Peng, W.; Zhang, Y.; Zhang, S.; Liu, X. Experimental study on the inhibition effect of water mist containing additives on the thermal runaway of lithium battery. *Process Saf. Environ. Prot.* **2024**, *182*, 999–1007.
15. Xiao, X.; Chen, B.; Jin, X.; Zeng, Q.; Tian, Y.; Li, Q. Experimental Study on the Effect of Synergistic Extinguishing Method Based on Liquid Nitrogen on Lithium-Ion Battery Fire After Thermal Runaway. *Fire* **2024**, *7*, 479. [[CrossRef](#)]
16. Zhang, L.; Li, Y.; Duan, Q.; Chen, M.; Xu, J.; Zhao, C.; Sun, J.; Wang, Q. Experimental study on the synergistic effect of gas extinguishing agents and water mist on suppressing lithium-ion battery fires. *J. Energy Storage* **2020**, *32*, 101801. [[CrossRef](#)]
17. Xu, J.; Guo, P.; Duan, Q.; Yu, X.; Zhang, L.; Liu, Y.; Wang, Q. Experimental study of the effectiveness of three kinds of extinguishing agents on suppressing lithium-ion battery fires. *Appl. Therm. Eng.* **2020**, *171*, 115076. [[CrossRef](#)]
18. Ye, C.; Liu, J.; Zhang, Q.; Jin, X.; Zhao, Y.; Pan, Z.; Chen, G.; Qiu, Y.; Ye, D.; Gu, L.; et al. Activating Metal Oxides Nanocatalysts for Electrocatalytic Water Oxidation by Quenching-Induced Near-Surface Metal Atom Functionality. *J. Am. Chem. Soc.* **2021**, *143*, 14169–14177. [[CrossRef](#)]
19. Luo, D.; Ding, X.; Hao, X.; Xie, H.; Cui, J.; Liu, P.; Yang, X.; Zhang, Z.; Guo, J.; Sun, S.; et al. Ni/Mn and Al Dual Concentration-Gradients To Mitigate Voltage Decay and Capacity Fading of Li-Rich Layered Cathodes. *ACS Energy Lett.* **2021**, *6*, 2755–2764.
20. Wang, Z.; Zhao, Q.; Yin, B.; Zhai, H.; Wang, J.; An, W. Characterization of fire behaviors associated with a thermal runaway in large-scale commercial $\text{LiNi}_{0.8}\text{Co}_{0.1}\text{Mn}_{0.1}\text{O}_2$ /graphite cells under external ignition. *Case Stud. Therm. Eng.* **2023**, *47*, 103126. [[CrossRef](#)]
21. Gong, Z.; Gu, C.; Sun, J.; Wang, H.; Li, Y.; Zhou, X.; Jia, Y.; Han, D. Experimental study on thermal runaway characteristic and residue of $\text{Li}(\text{Ni}_{0.8}\text{Co}_{0.1}\text{Mn}_{0.1})\text{O}_2$ lithium-ion batteries induced by overcharge. *J. Energy Storage* **2023**, *68*, 107705.
22. Borchers, A.; Pieler, T. Programming pluripotent precursor cells derived from Xenopus embryos to generate specific tissues and organs. *Genes* **2010**, *1*, 413–426. [[CrossRef](#)]
23. Jia, Z.; Qin, P.; Li, Z.; Wei, Z.; Jin, K.; Jiang, L.; Wang, Q. Analysis of gas release during the process of thermal runaway of lithium-ion batteries with three different cathode materials. *J. Energy Storage* **2022**, *50*, 104302. [[CrossRef](#)]
24. Li, H.; Lu, J.; Wang, J.; Yang, L. Study on extinguishing performance and suppression mechanism of thermal runaway combustible gas flame of lithium battery by $\text{NH}_4\text{H}_2\text{PO}_4$ water mist. *Case Stud. Therm. Eng.* **2025**, *71*, 106208.
25. Chang, C.; Wang, R. Experimental investigation of thermal runaway behaviour and inhibition strategies in large-capacity lithium iron phosphate (LiFePO_4) batteries for electric vehicles. *Int. J. Electrochem. Sci.* **2024**, *19*, 100877.
26. Pastor, J.V.; García, A.; Monsalve-Serrano, J.; Golke, D. Analysis of the aging effects on the thermal runaway characteristics of Lithium-Ion cells through stepwise reactions. *Appl. Therm. Eng.* **2023**, *230*, 120685. [[CrossRef](#)]
27. Li, L.; Bian, Y.; Zhang, X.; Guan, Y.; Fan, E.; Wu, F.; Chen, R. Process for recycling mixed-cathode materials from spent lithium-ion batteries and kinetics of leaching. *Waste Manag.* **2018**, *71*, 362–371.
28. Wang, K.; Ouyang, D.; Yuan, S.; Wu, D.; Zhang, J.; Chang, C.; Yan, K.; Sun, H.; Qian, X. Experimental study on inhibition effect of Novec-1230 on thermal runaway fire of lithium-ion battery packs induced by overcharging. *J. Energy Storage* **2025**, *120*, 116451. [[CrossRef](#)]
29. Sloop, S.E.; Crandon, L.; Allen, M.; Lerner, M.M.; Zhang, H.; Sirisaksoontorn, W.; Gaines, L.; Kim, J.; Lee, M. Cathode healing methods for recycling of lithium-ion batteries. *Sustain. Mater. Technol.* **2019**, *22*, e00113. [[CrossRef](#)]

30. Zhang, L.; Jin, K.; Sun, J.; Wang, Q. A Review of Fire-Extinguishing Agents and Fire Suppression Strategies for Lithium-Ion Batteries Fire. *Fire Technol.* **2022**, *60*, 817–858.
31. Wang, F.; Sheng, H.; Li, W.; Gerken, J.B.; Jin, S.; Stahl, S.S. Stable Tetrasubstituted Quinone Redox Reservoir for Enhancing Decoupled Hydrogen and Oxygen Evolution. *ACS Energy Lett.* **2021**, *6*, 1533–1539. [CrossRef] [PubMed]
32. Bonilla, M.; Kolekar, S.; Ma, Y.; Diaz, H.C.; Kalappattil, V.; Das, R.; Eggers, T.; Gutierrez, H.R.; Phan, M.H.; Batzill, M. Strong room-temperature ferromagnetism in $\text{VSe}_{(2)}$ monolayers on van der Waals substrates. *Nat. Nanotechnol.* **2018**, *13*, 289–293. [CrossRef] [PubMed]
33. Winter, L.R.; Chen, J.G. N_2 Fixation by Plasma-Activated Processes. *Joule* **2021**, *5*, 300–315. [CrossRef]
34. Huang, Z.; Li, X.; Wang, Q.; Duan, Q.; Li, Y.; Li, L.; Wang, Q. Experimental investigation on thermal runaway propagation of large format lithium ion battery modules with two cathodes. *Int. J. Heat Mass Transf.* **2021**, *172*, 121077. [CrossRef]

Disclaimer/Publisher’s Note: The statements, opinions and data contained in all publications are solely those of the individual author(s) and contributor(s) and not of MDPI and/or the editor(s). MDPI and/or the editor(s) disclaim responsibility for any injury to people or property resulting from any ideas, methods, instructions or products referred to in the content.